# MSR-ERO : NARROW ANGLE NAVIGATION CAMERA

**Pierre Goux[(1)], Antoine Lecocq[(1)], Michael Richert[(1)], Alex Marchand[(2)], Keyvan Kanani[(2)], Manuel Sanchez-Gestido[(3)]**

[(1)]*Sodern, ArianeGroup, 20, Avenue Descartes, 94450 Limeil-Brévannes, France*
[(2)]*Airbus Defence & Space, 31, Rue des Cosmonautes, 31400 Toulouse, France*
[(3)]*ESA, ESTEC, Noordwijk, The Netherlands*

## ABSTRACT

The Mars Sample Return (MSR) – Earth Return Orbiter (ERO) is a European Space Agency contribution to the ESA/NASA joint Mars Sample Return Campaign, which aims to return soil and atmospheric samples from the Mars surface to Earth by 2031. The ERO orbiter will have to detect, rendezvous with, and capture a football-size object called the Orbiting Sample (OS); a passive, inert, non-cooperative and uncontrolled toppling object in Mars orbit. Such a challenging acquisition and tracking phase requires a visual detection involving the use of a long-range detection camera which Sodern has been selected by Airbus Defence and Space for supplying and is referred to as Narrow Angle Camera (NAC). The NAC is meant to take images of the Orbiting Sample (OS) and stars in the vicinity of Mars, during both an initial OS detection phase, as well as provide Target Centre of Brightness data during the Rendezvous phase of the MSR-ERO mission. This phase makes use of an algorithm, called Target Centroiding, which is designed to resist solar flares, straylight, and motion, and restitutes the OS line of sight while resisting potential outliers. This paper describes the current features of the NAC and ongoing activities, with a focus on architecture, design and simulation. A first section presents on the overall camera architecture and modelling, and is followed by an overview of the rendezvous phase design. The third and last sections focus on the NAC preliminary performance evaluations in both phases as well as development plans, ongoing testing and future works.

## 1 INTRODUCTION

Earth Return Orbiter (ERO) is a European participation to the international Mars Sample Return (MSR) program. The NASA Perseverance rover will collect samples on Mars surface and let them on planet surface for later retrieval. The NASA built Sample Retrieval Lander (SRL) will arrive on Mars surface in 2028. Drones will retrieve and collect samples left by Perseverance rover and carry them back to SRL. About 30 samples will be sealed inside a 30 cm container, named Orbiting Sample (OS). The OS will be launched by a rocket: the Mars Ascend Vehicle (MAV) which is on-board the SRL. ERO will be launched in 2027, with a back-up launch window in 2028. ERO will be used as a radio relay for Perseverance and SRL. Its role after MAV launch in 2031 is to retrieve and capture the OS. For this purpose, ERO is equipped with 2 Narrow-Angle Cameras (NAC) aiming to detect the football ball size OS from as far as 3 000 km. The NAC is assembled on the CCRS (Capture, Containment and Return System) which is a payload provided by NASA. During the OS detection phase, Mars limb induces Straylight in the NAC and makes the detection very challenging. The raw NAC pictures shall be analyzed on ground to retrieve the OS in front of the background of stars. The NAC shall also be used during the OS rendezvous phase, by providing OS centroiding values to the

on-board computer (OBC) until a distance down to 400m. Once captured, the OS shall be sealed inside the Earth Entry Vehicle (EEV). About 50% of the mass of the CCRS, including the two NACs, should be jettisoned around Mars. ERO should return to Earth with its Mars soil samples in 2031.

**Mission environment, specifics and sensor constraints** ERO's orbit is currently designed to be in close proximity to the surface of Mars, orbiting at an altitude of approximately 300km. While the Mars Ascend Vehicle will be launched in order to minimize the detection phase duration, the NAC must still be designed to undergo various scenarios, including unfavorable ones. Specifically, both ERO and the OS being in low Mars orbit, Mars and its limb will occupy a large portion of the hemisphere in front of the camera and the edge of the limb will be close to the line of sight, adding considerable straylight to an already challenging detection of a faint object. The NAC includes a baffle to prevent straylight from reaching the detector. The amount of light entering the baffle due to the Sun is up to about 8W, while the total power from Mars can reach up to about 1.8W in some scenarios [25], which makes the baffle a critical element to ensure NAC SNR performance. In addition, due to the high statistical fluctuations of thermal constraints for cruise to Mars and Mars orbits, the NAC must also resist highly variable thermal environment. The NAC is mounted directly on the CCRS panels, close to pyrotechnic actuators, and is thus being submitted to high random vibrations levels due to launch acoustics, and shock due to actuators. One of the two NACs is located a few tens of centimeters from ERO's main UHF communication antenna. The EMC constraints on the NAC are very strict, to prevent radiated emissions from the communication between the NAC and to OBC from disrupting the UHF communication. Finally, due to the potential duration of the mission and rendezvous phases, including back-ups and re-routings, the NAC must endure difficult end of life conditions, both in terms of radiative environment and radiative dose, contamination, and direct exposure to Sunlight.

## 2 NARROW ANGLE CAMERA OVERVIEW

The ERO NAC camera is based on HORUS [26], [27], a new single-box star tracker already selected by Airbus Defence & Space for its GEO satcom. Sodern has also recently developed a Navigation Camera designed for the harsh environment of the recently-launched JUICE Mission, which feedback and experience greatly helps in developing the NAC. [18], [24]
The NAC uses the focal plane assembly (including detector, board and thermo-electric cooler) and the power supply from HORUS. The NAC baffle, optical assembly, processing board (including FPGA and SDRAM) and VHDL were developed specifically for this application. The NAC development also includes specific ground support equipment to verify the performances of the camera, especially Straylight.
The NAC is used to autonomously take pictures of foreground OS target object, which is anticipated to be located at several hundreds to thousands of kilometers away, against a background of more distant stars. To this end, the NAC delivers raw full frame images in imaging mode and centroiding (or brightness center) of the unresolved OS target in target mode. The NAC is also used during the early phase of the rendezvous, down to a distance of 400m. For short-distance rendezvous, information from Lidars is used, and the NAC still continue to provide centroid information down to 20m. At short distance, the OS target becomes resolved but however the method for image processing and centre computing remains similar.

### 2.1 Operational Architecture and Mission phases

The ERO Narrow Angle Camera offers three main operating modes:

- A STAND-BY mode

- An IMAGING mode, tailored to the long-range detection phase
- A TARGET CENTROIDING (TgC) mode, tailored to the rendez-vous phase

When the NAC approaches the OS, the TARGET CENTROIDING mode is used to deliver the OS centroid, on regular basis, to the ERO Navigation system. The TARGET CENTROIDING mode can be used from OS distances up to 300km and performance is guaranteed from 70km down to 400m.

### 2.2 Optical & Mechanical design

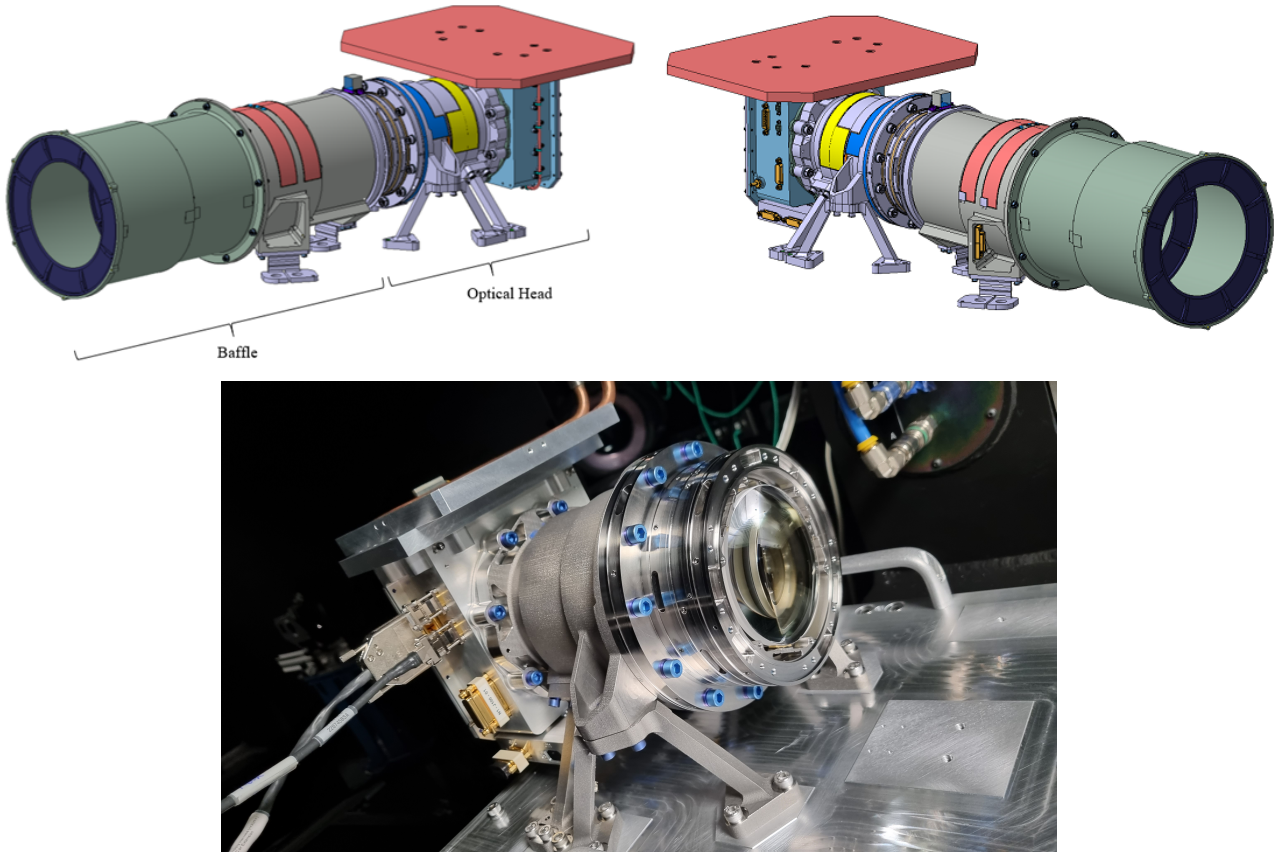


Figure 1: Narrow Angle Camera 3D Views (top) and EM model without baffle (bottom)

The accommodation of the NAC opto-mechanical assembly is presented hereafter on Figure 1. The camera is designed in two main sub-assemblies: the baffle, which protects the camera from Straylight from Mars Limb and Sun, and the optical head, including a focal plane assembly based on the FaintStar2 CMOS detector, and a specific lens assembly.
The baffle is essential to maintain the high signal-to-noise ratio (SNR) necessary to detect the OS. This cylindrical shaped baffle is customized considering the lens optical layout and the requirement of the location of the boresight from the Mars limb and the 30 degrees Sun exclusion angle. The baffle includes 5 black-coated vanes that form cavities and act as optical traps. When illuminated by the Sun, the baffle can get hot due to these black coatings. For this reason, a portion of the external surface of the baffle is coated with high-emissivity tape to evacuate heat. Due to its length, and for mechanical reasons, the baffle is a separate sub-assembly and is directly mounted on the NAC baseplate, using standoffs in an effort to minimize heat conductivity to the baseplate. The optical head includes a dioptric lens assembly composed of 11 lenses. Considering the ERO environment,

the optical layout is based on radiation tolerant glasses, including some glasses developed specifically for Sodern and used in Star Tracker manufacturing. The first lens is manufactured in fused silica for ionizing radiation shielding.
A good control of the Point Spread Function (PSF) is necessary to ensure OS detection. For this reason, each individual lens is assembled in an optical mount, which position is adjusted during assembling operation. The NAC optical mounts inherit the recent development of ultra-stable optical mounts, developed and qualified by Sodern for the UV2VIS Spectrometer in the frame of the Sentinel 5 mission which is part of the European Earth Observation Programme "Copernicus". A view of the NAC lens assembly is provided in Figure 2.

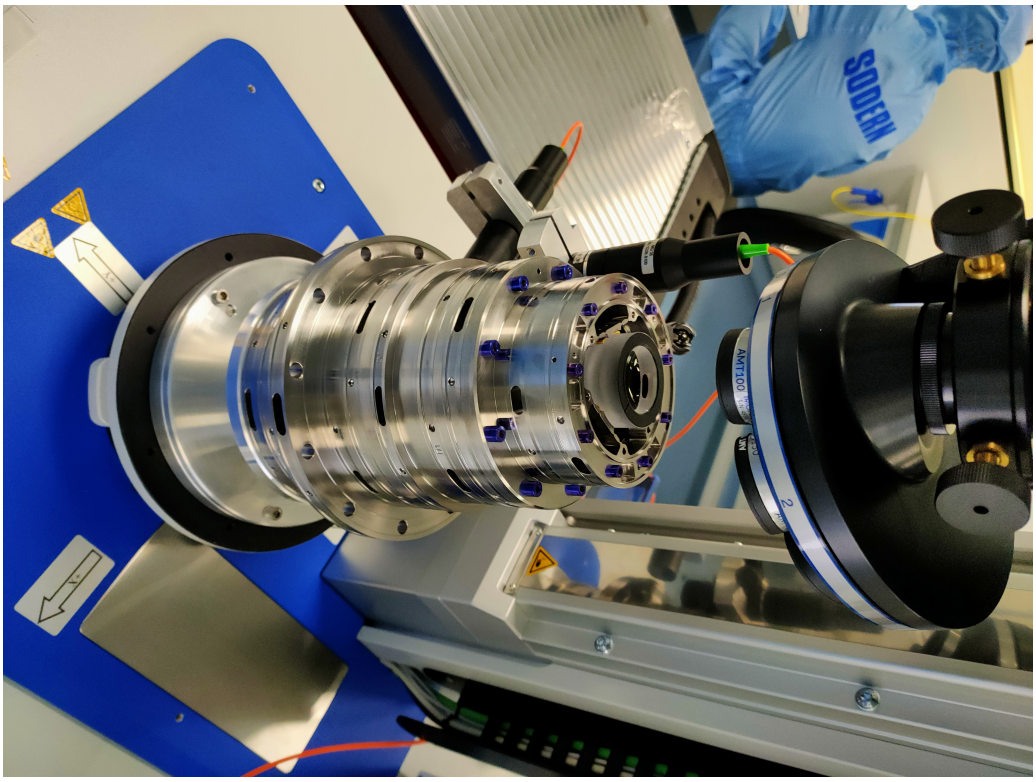


Figure 2: View of the NAC EM lens assembly during final measurements

The whole mechanical assembly is provided with a master reference cube implemented on the top of the optical module for on-ground correct placement and alignment of the camera boresight axis into the orbiter. The mechanical interface of the optical module is ensured through three kinematics bipod flexures in Titanium, to ensure thermal decoupling from the NAC baseplate. The NAC Electronic box (see Figure 3) is based on the FaintStar2 monochrome, 1 Mega-pixel CMOS Image Sensor. The image sensor is assembled on a thermo-electric cooler (TEC) to ensure a sufficiently low temperature to minimize the impact of dark signal and defective pixels (hot pixels due to radiations) during the mission. The E-box includes three PCBs: one for the image sensor, one for FPGA, SDRAM and SpaceWire communication, and one for Power Supply of all NAC elements. These three boards are assembled in an aluminum housing using a specific mounting technique, already validated on star trackers, that yields exceptional thermal and mechanical stability over operational environments.
In this standalone camera, the numerical functions of the electronic assembly allows to perform in parallel the image sensor sequencing and centroid computing, as well as the thermal control of the detector and communication with the OBC, using a single FPGA. The thermal control of the camera is fundamental and consists of active control elements to maintain image sensor and optical module within a controlled range of temperature throughout the mission. It is also necessary to ensure low

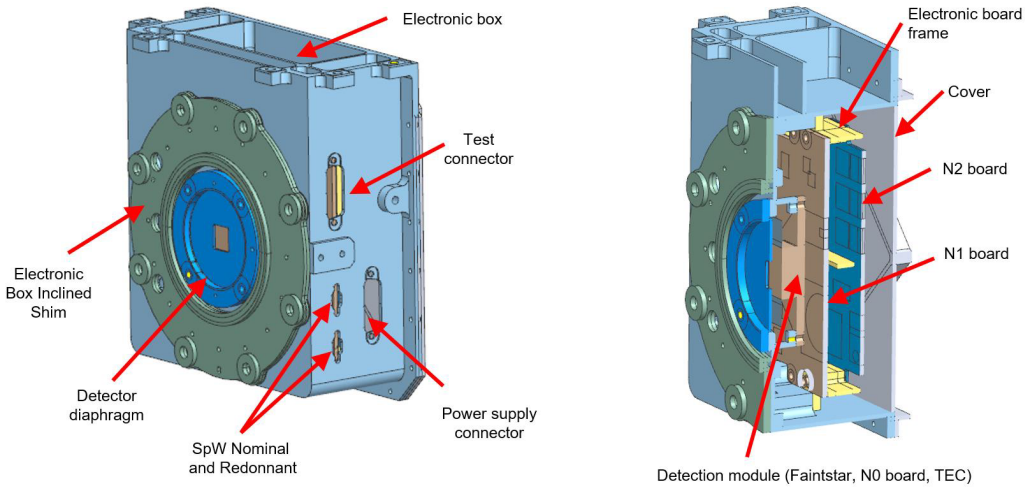


Figure 3: Electronic Box Design

spatial temperature gradients between lenses with a resulting temperature in orbit foreseen to be around 20 degrees, close to the one used for calibration on ground at Sodern premises. The NAC includes 3 independent heating lines (one for the electronic box, one for the lens assembly, one for the baffle), each line including heaters and thermal sensors. The control loop of these heating lines is implemented on ERO. The camera includes two radiative surfaces: a radiator is fixed on the electronic unit to dissipate heat from the NAC boards, and a specific low emissivity coating is implemented on the baffle to dissipate heat due to exposure to Sun. Moreover, Airbus Defence and Space will implement a thermal insulation (Multi-Layer Insulation) of the overall camera to protect the NAC from orbiter and external space environment. The main characteristics of the NAC are summarized in Table 1.

| Parameter | Value |
|---|---|
| Image sensor | FaintStar2 |
| Matrix size | 1020x1020 |
| Pixel encoding | 12 bits |
| Camera field of view (circular) | 4,5deg(*) |
| Extended field of view | 4,5 x 4,5deg(*) |
| Lens focal length | 129mm |
| Lens entrance pupil diameter | Ø80mm |
| Baffle exclusion angle | 14deg |
| Power supply | 28V power bus |
| Power consumption – Stand by (TEC OFF) | <5W |
| Imaging and Target Centroiding modes (TEC ON) | <12W |
| Data interface | Redounded Spacewire link |
| Operating modes | STAND BY ; IMAGING ; TARGET CENTROIDING ; |
| Integration time (Imaging mode) | 241 us to 30 s |

(*) Performances guaranteed in circular Field of View

Table 1: NAC characteristics & evaluation results

## 3 DETECTION PHASE

To assess NAC performances in this far-range scenario, we use a modelling of the Orbiting Sample and derive a Signal-to-Noise ratio, examining all potential contributors. Images are then processed on ground by Airbus Defence & Space, to assess presence of the Orbiting Sample during the mission trajectory, and prepare the follow-up rendezvous phase.

### 3.1 OS Modelling

The Orbiting Sample, as designed by NASA/JPL at the time of writing is a 229 mm x 184 mm cylinder, as illustrated in Figure 4 in renderings.

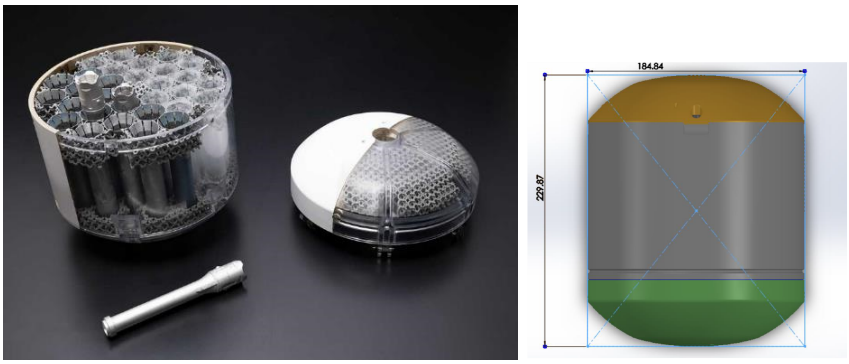


Figure 4: Orbiting Sample Renderings (Credits NASA/JPL)

Its apparent magnitude can be computed by:

$$m_{app} = -5\log_{10}\left(\frac{D\sqrt{A}}{1329\times10^3}\right) + 2.5\log_{10}\times \left(\frac{d_{OS}^2 d_{ON}^2}{\frac{2}{3}\left(\left(1-\frac{\varphi}{\pi}\right)\cos\varphi + \frac{1}{\pi}\sin\varphi\right)\times(1.496\times10^{11})^4}\right) \quad (1)$$

Where D is the OS diameter, A its albedo, $d_{OS}$ is the distance OS to Sun, $d_{ON}$ the distance OS to NAC (all in meters) and $\varphi$ is the OS sun phase angle. Considering the optical properties of the OS can vary depending on its attitude and the latter is not fully consolidated, magnitudes and fluxes were computed for a diffuse Lambertian sphere of diameter 28cm and albedo 0.37. A nominal target magnitude for design was set at 12.6. This corresponds to 1000km from target at a solar phase angle of 120deg, up to 3000km for a solar phase angle of 0deg.
The sun phase angle is limited to 150deg. With Sun angle equal 180deg, the target is not illuminated on the side seen by the NAC and the sun is in the NAC field of view : no detection would be possible. Considering a SEA of 30deg, the sun angle for the OS is never greater than 150deg (180deg-SEA) during the detection and proximity phase. The target 12.6 apparent magnitude for detection corresponds to a photonic flux of 6171,7 Photons/s in the camera's aperture.

### 3.2 Straylight Simulation

In order to validate the design before any test could be conducted, Straylight simulations were run in specialized software, FRED from Photon Engineering. Simulations have been used for 3 purposes: confirmation of the design hypotheses, computation of the performances of the NAC system and finally comparison of the simulation with real world per-formances. For the specific very-low levels

of straylight to be simulated for the NAC, Sodern developed a specific simulation method enabling to optimize computer calculation resources [25]. In the frame of the NAC project, Sodern provides Airbus with an accurate Straylight model that enables the calculation of straylight levels induced on the detector, depending on scenes in the hemisphere in from of NAC, that can include Sun, Mars Limb and/or ERO structure.

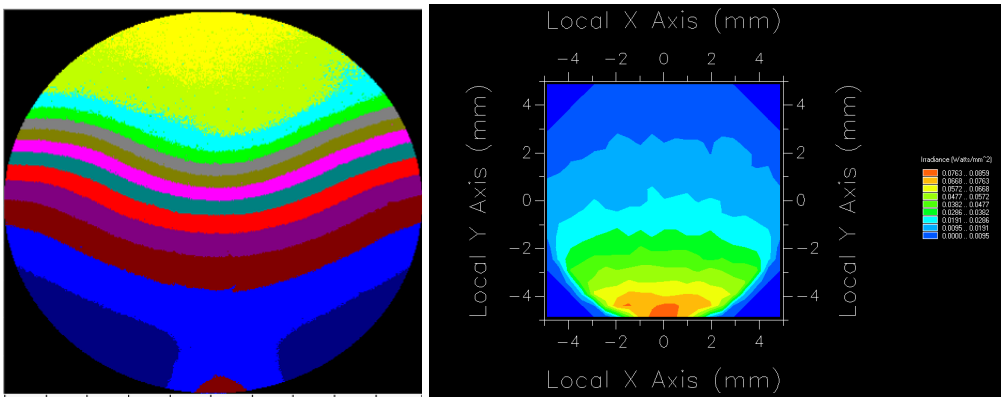


Figure 5: Straylight Irradiance: comparison of real measurements on a prototype (left) with simulations (right)

The results of the straylight simulation were compared with existing test and real operation data from star trackers, and showed good correlation, as shown Figure 5

### 3.3 SNR Performances

We define the Signal-to-Noise Ratio (SNR) as the ratio between the maximum signal collected by one pixel value over the local noise standard deviation, considering that local noise excludes protons and stars and includes all other noise contributors, in particular but not limited to Photo-Response Non-Uniformity (PRNU), dark current and Dark Signal Non-Uniformity (DSNU), photonic noise (in particular due to straylight), electronic and readout noises. The SNR of an image is considered as acceptable only if the probability of having a given pixel lit by a proton less than 1% for more the worst week solar flare scenario during a 2s integration time. The SNR is be considered in worst case configuration where the target is at the corner of 4 pixels.

The main noise budget contributor is by far the straylight. On average :

- The Mars Limb Exclusion Angle (MLEA) accounts for 53% of total noise, on top of its PRNU (11%), and its local non-uniformity (10%)
- Sun Eclusion Angle contribution is however limited (roughly 2%)
- Meanwhile, detector noises are minimized (Temporal Noise of detector is 11% fo total noise, signal PRNU is 10%, and FPN contributes to around 5% of the total noise budget

We present a table of SNR performances in Table 2. Several major straylight cases have been identified, two of which are recalled here, from [25]. In Table 2, Case A corresponds to a Mars Limb Exclusion Angle of 13.5deg and a solar phase angle of 90deg and Case B, a MLEA of 13.5deg and a solar phase angle of 120deg.
Using in-house simulation tool ATOS, described in further sections, we can obtain the Figure 6 illustration of a typical image taken by the NAC, under in-flight assumptions (in terms of noise, starlight & straylight and radiations).

Table 2: SNR performances in Imaging Mode

| Magnitude | Case A Average | Case A Max | Case B Average | Case B Max |
|---|---|---|---|---|
| 12.6 | 4.82 | 4.36 | 4.71 | 3.86 |
| 12.06 | 7.68 | 6.98 | 7.51 | 6.23 |
| 11.26 | 14.82 | 13.64 | 14.53 | 12.32 |
| 10.42 | 27.54 | 25.88 | 27.15 | 23.90 |

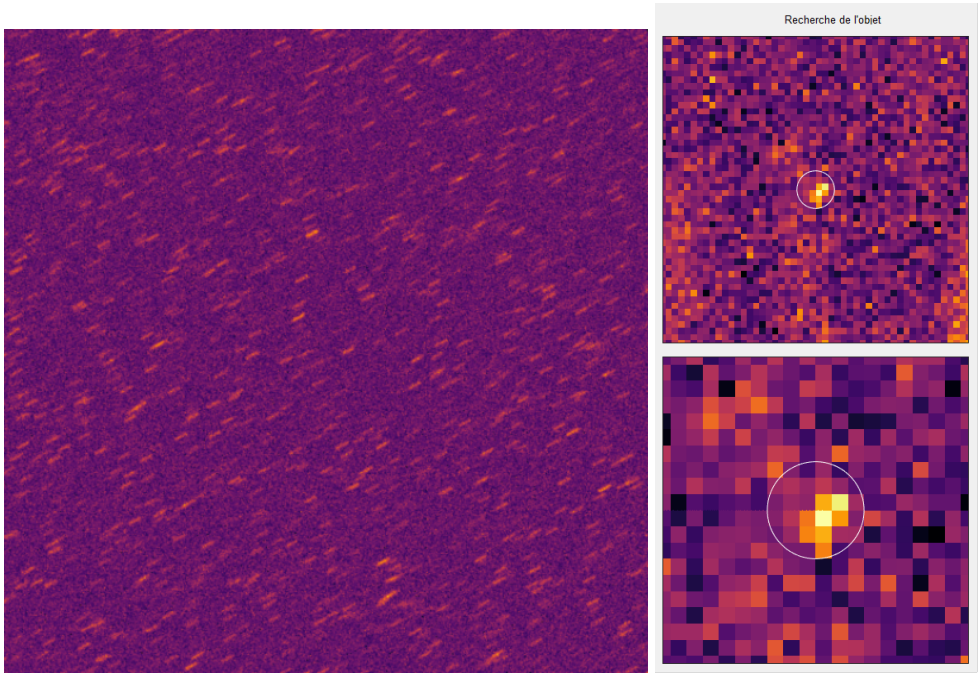


Figure 6: Simulation of a typical OS image at 1200km (log scale)

## 4 RENDEZ-VOUS PHASE

This phase's purpose is to retrieve images, as well as both accurate enough and sufficiently reliable centroid data from the Target, in order to for an efficient rendezvous. A modelling and simulation approach has been selected, alongside a careful analysis of the assumptions used and their justifications is foreseen by elementary test with:

- Characterisation of the relevant stray light background on the image sensor in a vacuum test set-up (vacuum is mandatory due to the rejection requirement level).
- Characterization of the FPA noise and non-uniformities with no light or with flat field illumination.
- Characterization of image quality through the measurement of the PSF, transverse spatial variation of the amplitude of the image received at the detector plane. This measurement is achieved in a test facility with a two-axis table equipped with a thermal chamber and a point source collimator. Indeed, PSF is function of optical aberration, detector features, assembly tolerances and also, but less dominant, the overall thermal regulation behaviour.
- Characterization of geometrical performances in the field of view in a similar test setup.

Thanks to our own heritage on star tracker, our in-house simulation tool, using a Monte-Carlo approach [5], allows predicting centroiding performance [21], [23]. This simulation includes all NAC

features that drive the end of life performance including FPA artefacts induced by ionizing radiation, and is presented in a subsection below. Beyond the initial proof of concept by simulation and in order to more realistically check the NAC capability, functional tests will be conducted on ground in the real night sky environment and with Earth pointing satellite assessment. Regarding environmental tests, Sodern has its own facilities as shakers and thermal vacuum chambers ; for Electro-Magnetic Interference and Compatibility testing, Sodern has a specific agreement with a supplier.

### 4.1 Target Centroiding Processing Overview

The process itself consists of the five following steps.

1. *Windowing*, allowing for an optional reduction of the processing to a known or estimated region of interest

2. *Masking*, of stars, defective pixels or other static perturbations identified during either ground or in-flight calibrations

3. *Thresholding*, to derive a reduced family of pixels likely to contain the Orbiting Sample, using models and look-up tables to predict its size and signal depending on mission parameters (distance, solar phase angle). This step is designed to be robust to random attitude, OS toppling, background noise and straylight.

4. *Filtering Protons*, from this resulting family of pixels. This step ensures consistency between lit pixels originating from the selected family most likely to contain the Orbiting Sample

5. *Centroid and Quality Index computations*, to ensure the detection of measurement outliers, and to provide insight to the OBC flight filter to quantify the likelihood of correctness of measurement.

Step 2. requires that several stars be masked to ensure the overall processing manages to isolate the OS family of pixels and compute its centroid. Correct positioning of those masks is crucial to the success of the algorithm, so as to not mistake a stable high-magnitude star to be confused for the OS. To evaluate the number of masks necessary, a star catalogue has been constructed, as described in the next section.

### 4.2 Star Catalogue

To generate a covering star catalogue, we need to begin by choosing sources. Out target covering magnitude is the highest V-band magnitude reachable by the OS in this phase, which is around 9.5 (for a 70km distance and a 120$\mathrm{deg}$ solar phase angle). The Tycho2 catalogue should therefore have sufficient star density coverage, since it reaches 99% completion for magnitude 11V. For completion, star density coverage, proper motion correctness and spectral type coverage, we have selected Tycho2 as a base Catalogue for our astronomical catalogue, among others for spectral type coverage, to derive instrumental magnitude.
From this astronomical catalogue, we know have to integrate the NAC characteristics, in order to determine instrumental magnitude from photometric calibrations, as well as concatenate close and bright stars for realism purposes. To sum up this work, we propose the flowchart on Figure 9. Converting visual magnitude to instrumental magnitude mainly uses the spectral response of the NAC, i.e. the product of the spectral transmission of the optics by the quantum efficiency of the detector. Photometrical conversion is established from the G&S [13] and INGS [1], [14], [16] catalogues, containing absolute spectral fluxes for several stars.

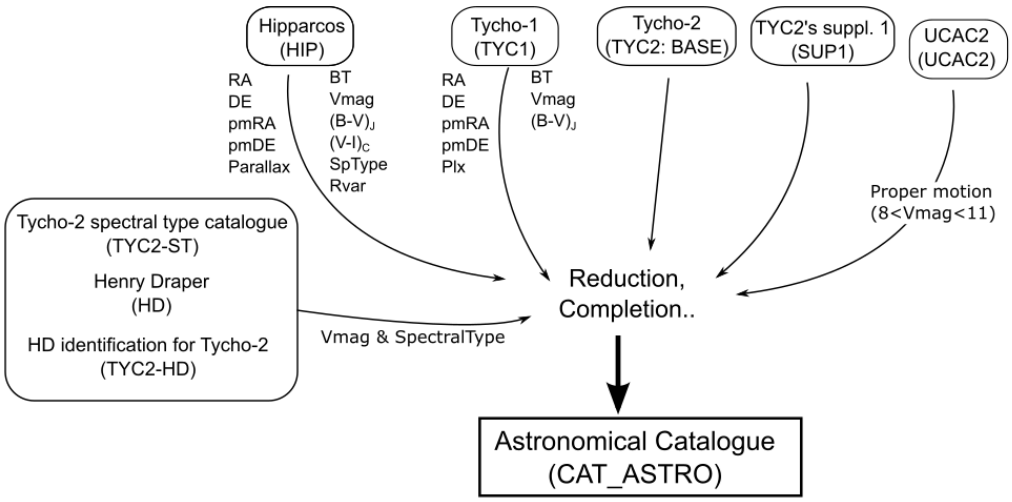


Figure 7: Astronomical Catalogue Construction Flowchart

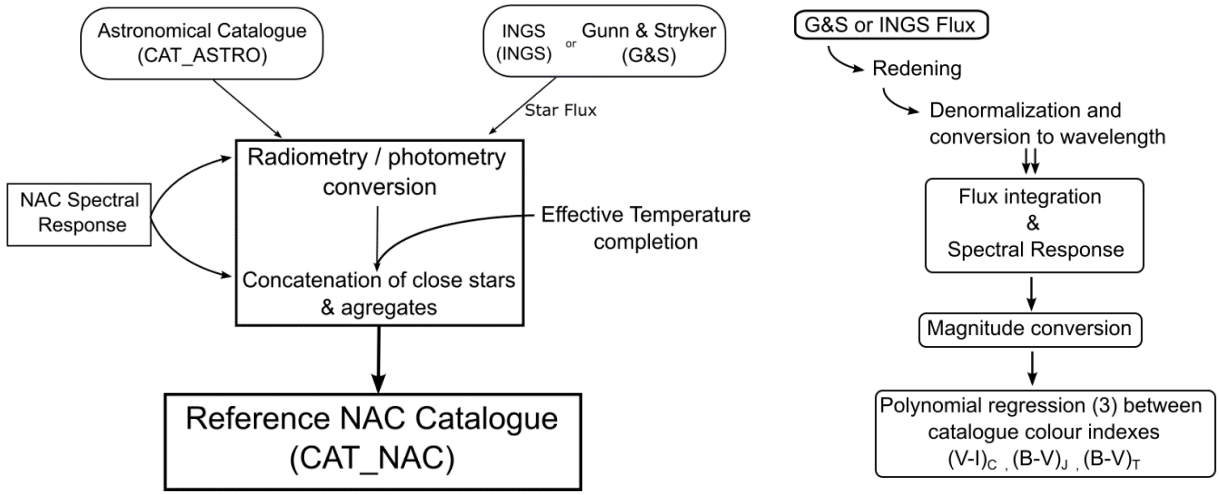


Figure 8: Left, Instrumental Magnitude Determination. Right, Colour Index Calibration Flowchart

G&S [13] fluxes needs be reddened, because interstellar dust contribution, which tends to redden their spectra is corrected from in the catalogue. This reddening needs to be restored, because it will be seen by the NAC. The corresponding magnitude error has been computed to be at most 0.03mag.

The colour indexes $(V-I)_C$ and $(B-V)_J$ are not know for every single star of CAT_ASTRO, hence the need for a third calibration law revolving around the well-known $(B-V)_T$ index. [2], [9]
In terms of confidence index and precision, those photometric indexes should be ranked in the following order : $(V-I)_C$ , then $(B-V)_J$ , and then $(B-V)_T = BT - VT$. Figure 7 below present our flowchart for instrumental magnitude determination, inspired from [3], [7]. Our normalization convention for integrating fluxes is based on a 6000K blackbody with equivalent luminosity to that of Vega.
The Figure 9 projections make use of the HEALPix sky tessellation, Hierarchical Equal Area isoLatitude Pixelation (of a sphere) tool [10]. We also acknowledge the VizieR data base [8].

Assuming an integration time of 50ms, i.e. a half-pixel cross-track, we can derive a link between a

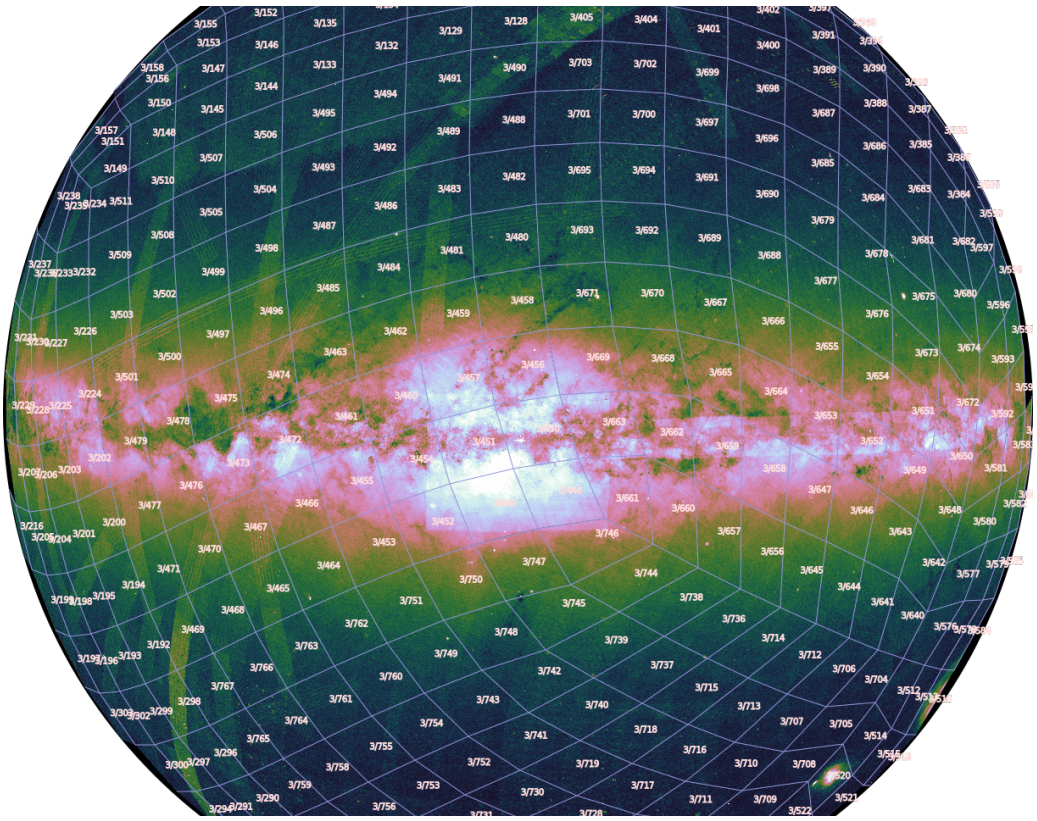

Figure 9: Density map of the celestial vault as seen by the NAC

target SNR, e.g. 4 and an Instrumental magnitude, in that case 9.3. The following Figure present the number of stars with a SNR higher than 4 over the celestial vault (0.1deg scanstep). The order of magnitude of the minimum number of visible stars with SNR higher than 4 is around 25, with probabilities of reaching 100 stars around 50%, and a typical high number of stars of roughly 250.

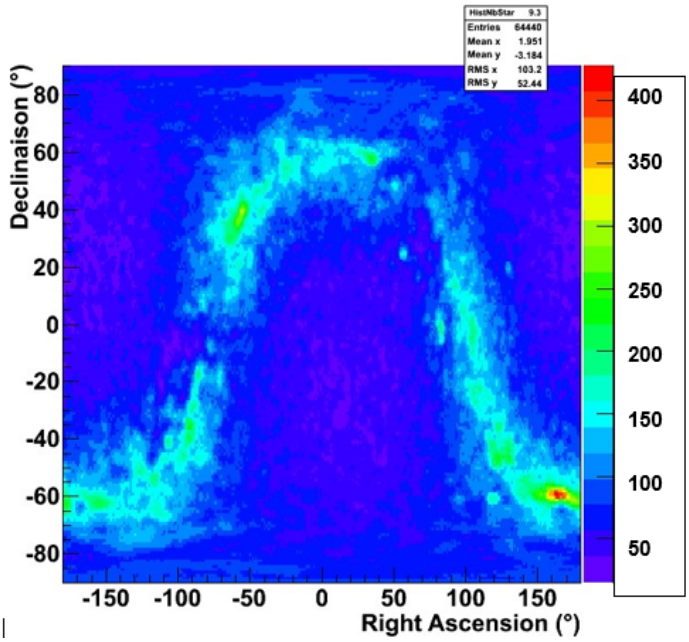


Figure 10: Distribution of the number of stars with a SNR above 4 for the NAC

A covering provision of masks has therefore been selected for the Masking phase of the Target Centroiding Algorithm. This would include stars as well as defective pixels and dark current spikes.

### 4.3 ATOS Simulation : Modelling & Methodology

ATOS (Assessment Tool for Optical Sensors) is a SODERN internal tool, which main uses are simulation and image processing, analysis and performance evaluations for those images, as well as specific processes and dedicated analyses. ROOT is an object-oriented program and library developed by the European Organization for Nuclear Research (CERN), under LGPL/GPL license. It is mainly used for its analysis features, histogramming, fitting, statistical studies, visualisations, as well as standard mathematical functions.
For the Rendezvous phase performance evaluation, we will perform series of Target Centroiding simulation along the range of cases in which performance should be measured and characterized. Varying the input scenarios, we will observe and measure the behaviour of the resulting centroid, i.e. LoS quality, as well as monitor the quality index, and the composition of the Pixels of Interest (POI) family. For that purpose, the signal from proton-detector interaction is also stored in a separate image, to assess whether a pixel in the POI family is contaminated by a proton. The simulation occurs in the following steps. After selecting a distance and a solar phase angle for the Orbiting Sample, thus choosing a total flux and a spot, we select the integration time, as well as all others Target Centroiding-related parameters from previously determined look-up tables, and we :

1. Generate the corresponding Photonic Stimulus (given a Cross-Track Velocity, CTV)
2. Propagate this stimulus to the detector alongside noise models, and digitalize (read) it.
3. Apply the Target Centroiding Algorithm

In order to determine statistical variations, the looping method is the following. Prior to generating the Photonic Stimulus, the intra-pixel position of the OS, as well as the OS direction and orientation are uniformly drawn. Then, for a same photonic stimulus, various draws of spatial and temporal noises are randomly drawn.
In order to determine statistical variations, the looping method is the following. Prior to generating the Photonic Stimulus, the intra-pixel position of the OS, as well as the OS direction and orientation are uniformly drawn. Then, for a same photonic stimulus, various draws of spatial and temporal noises are randomly drawn. This process was repeated with seeded pseudo-random number generators, based on the Mersenne Twister [6] for noise maps generation.
The scenario list is designed to cover many distances from 300km down to 20m, several phase angles from 0° to 150°, motion up to 0.5°/s. In addition, the radiation fluence was set-up as a worst week solar flare condition, with end-of-life noise levels and space environment effects, and the detector temperature was regulated at -15°C. For each parameter set corresponding to a loop iteration, a performance evaluation is realized, using a double random draw:

- A random spatial noise draw, repeated several times
- For each spatial noise draw, several draws of temporal noise.

Spatial noise includes the following:

- Dark Signal Non-Uniformity, or DSNU, which is a gaussian component, alongside spikes, which are an exponential function of temperature

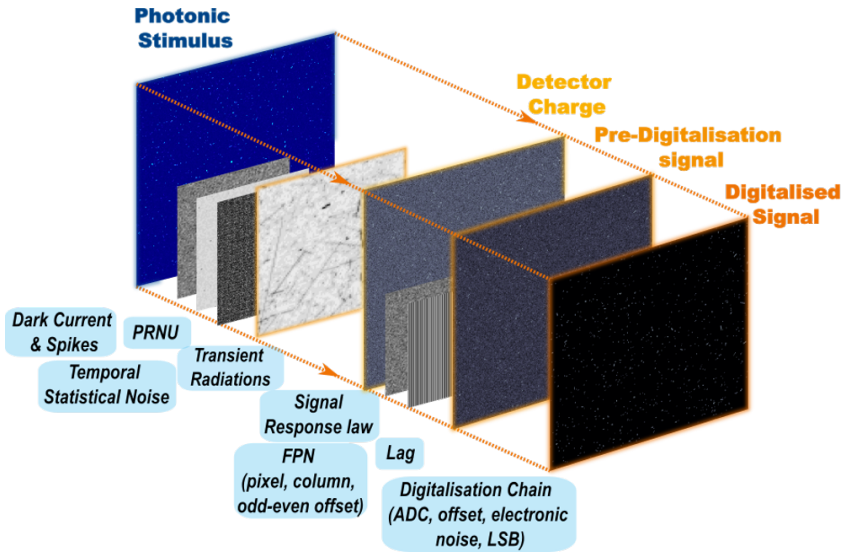


Figure 11: Overview of the Digitalization process in ATOS

- Photo Response Non-Uniformity, or PRNU, which revolves around the intrinsic sensitivity of each pixel.
- Random electronic noise, as well as zero-ADC, and fix pattern noises.

It is thus possible for each spatial draw to establish a statistic on the measured values (signal, position, etc.) and to compute a mean and standard deviation for this occurrence of spatial noise. Repeating this for each spatial noise draw allows the determination of two distributions:
(i) A distribution of mean values of temporal draws, over all spatial noise draws and
(ii) A distribution of standard deviation values of temporal draws, over all spatial noise draws.
The standard deviation of the former distribution gives the spatial noise: it is the fluctuation of the mean value over temporal draws, as a function of the spatial draw. Strictly speaking, there remains in this estimation a residue of a temporal component due to averaging over temporal draws, which heavily decreases when the number of temporal draws is large. This component can be inferred with the second distribution. The mean of the latter distribution gives the temporal noise: it averages the obtained temporal biases over all spatial draws. It is therefore a global average, hiding small fluctuations due to each spatial draw, i.e., correlation between the temporal noise, and a given configuration of spatial noise.

For statistical purposes, each parameter set has been considered across a 125 spatial x 125 temporal x 2 intra-pixel run, i.e. 62,500 images per parameter set per scene. This is enough to maintain sufficient precision to evaluate the TgC performance, since that leaves a highest possible ($1\sigma$) fluctuation of 0.1 µrad on LoS std. dev and bias values.
With the exception of the limit case @70km,120deg, each dot in the figure below, represents 1,250 runs of the Target Centroiding Algorithm. Dotted lines are the specified minimal and maximal fluxes for the corresponding distance/solar phase angle combination, so as to have at least 62,500 runs for each setting (with a grand total of several million images).

### 4.4 Performance results

Overall, we have found the Target Centroiding to provide very accurate in terms of LoS (requirement $< 25$µrad 3-$\sigma$ noise and bias) and availability ($< 10\%$of outliers) under worst week solar flare

conditions for the entire 400m to 70km range, for solar phase angles up to 120deg, and cross-track velocities up to 0.1deg/s, by some margin.
Our worst-case Faintest OS LoS performance was: Std : 11.8 µrad ; Bias : 11.5 µrad($\pm$ 0.1µrad) and our close-range worst-case lead to Std : 4.6 µrad ; Bias : 4.6 µrad($\pm$ 0.1µrad).

The performance of the Target Centroiding relies almost entirely on the choice of the integration time. Worst-case hypotheses constrain this integration time selection, and all other parameters are set accordingly. We present in Figure 12 an overview of the LoS performance over the extended range of distances and solar phase angles, for a 0.1deg/s CTV and worst week solar flare conditions:

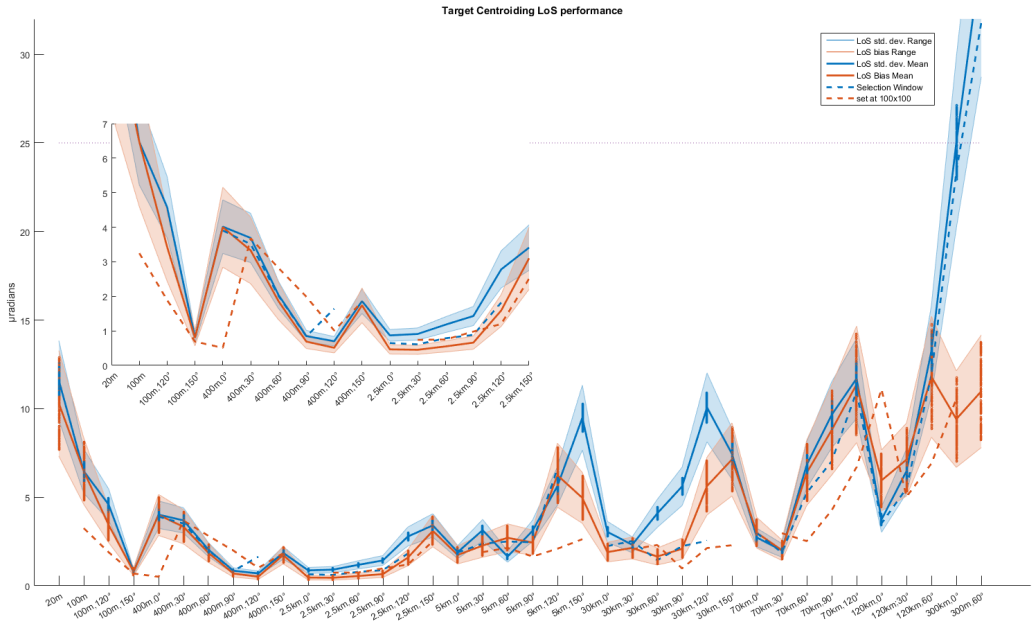


Figure 12: LoS performance (µrad, 3sigma) overview, for 0.1°/s CTV under worst week solar flare conditions

Moreover, the extended range characterization showed the Target Centroiding to also meet those requirements for distances between 20 to 400m, for phase angles of 150° up to 40 km, and otherwise for distances up to 220km (for phases $< 60°$), under the 0.1°/s CTV and worst week solar flare conditions. Relaxing the worst-week solar flare condition would allow for higher integration times compensating hard cases (high CTV, or high solar phase angles) and yield yet better performance, meaning that the Target Centroiding could be usable across a much wider range of distances than required. In addition, this study also found that the Target Centroiding was robust to cross-track velocities up to 0.5°/s and could withstand this CTV up to the 70km/60° case. This cross-track velocity is a limiting factor for higher distance/solar phase angle combinations, however, at close range it is rather unimpactful because of the low integration time. This leads us to believe that the Target Centroiding Algorithm can often be used reliably even for high CTV cases, provided the OS signal is sufficient. With regards to Quality Index rate and outliers, we found the TgC to be compliant to the requirement up to Full Frame. However, for 120km, or 300km cases, the necessity to increase integration time to compensate for the loss of signal is hardly compatible with the worst week solar flare conditions.
Relaxing this condition could allow for the TgC to meet the target requirements even way past the 70km/120° target, and across a broad range of fluxes, considering that the nominal proton flux is reduced by a factor of almost 25.

## 5 CONCLUSIONS

The two NAC cameras are key units aboard the MSR-ERO orbiter and will provide observation capabilities to detect and rendezvous and finally contribute to the capture the OS uncooperative target. The NAC development reaches in 2023 several key milestones of the development. After manufacturing of several mock-ups in the previous development phases (including shock mockups, detector characterization model and Lens Assembly mock-up), a fully representative Engineering Model (EM) camera is being assembled. This EM will undergo full performance testing, including Straylight test, EMC test and real-sky test. The NAC flight models, one protoflight model and one flight model 2, will be manufactured in 2024. The PFM will undergo qualification range environmental tests. Delivery of these camera to Airbus Defence and Space is planned Q4 2024.

## 6 ACKNOWLEDGEMENTS

Sodern is under contract with Airbus Defense & Space to design and manufacture the NAC ERO. It is part of the Mars Sample Return mission, a joint ESA/NASA program. ESA leads the Earth Return Orbiter project. We would like to thank Alex Marchand and the Airbus team, as well as Manuel Sanchez Gestido (ESA) for their inputs. The views expressed in this article can in no way be taken to reflect the official opinion of the European Space Agency.




## 7 SOFTWARE AND THIRD PARTY DATA REPOSITORY CITATIONS

`astropy` [15], [19] ; `Source Extractor` [4] ; and ADS's *Surrender* [20].

## REFERENCES

[1] D. Egret, B. J. M. Hassall, A. Heck, C. Jaschek, M. Jaschek, and A. Talavera, "The iue low-dispersion spectra reference atlas," in *Cool Stars with Excesses of Heavy Elements*, M. Jaschek and P. C. Keenan, Eds., Dordrecht: Springer Netherlands, 1985, pp. 47–52, ISBN: 978-94-009-5325-3.

[2] J. A. R. Caldwell, A. W. J. Cousins, C. C. Ahlers, P. van Wamelen, and E. J. Maritz, "Statistical Relations between the Photometric Colours of Common Types of Stars in the UBV(RI)c, JHK, and uvby Systems," *South African Astronomical Observatory Circular*, vol. 15, p. 1, Jan. 1993.

[3] F. Natali, G. Natali, E. Pompei, and F. Pedichini, "The use of the (B-I) color index and applications of the (B-I) versus (B-V) relationship I. Open clusters.," **??***jnlA&A*, vol. 289, pp. 756–762, Sep. 1994.

[4] E. Bertin and S. Arnouts, "SExtractor: Software for source extraction.," **??***jnlA&As*, vol. 117, pp. 393–404, Jun. 1996. DOI: `10.1051/aas:1996164`.

[5] R. Brun and F. Rademakers, "Root — an object oriented data analysis framework," *Nuclear Instruments and Methods in Physics Research Section A: Accelerators, Spectrometers, Detectors and Associated Equipment*, vol. 389, no. 1, pp. 81–86, 1997, New Computing Techniques in Physics Research V, ISSN: 0168-9002. DOI: https://doi.org/10.1016/S0168-9002(97)00048-X. [Online]. Available: https://www.sciencedirect.com/science/article/pii/S016890029700048X.

[6] M. Matsumoto and T. Nishimura, "Mersenne twister: A 623-dimensionally equidistributed uniform pseudo-random number generator," vol. 8, no. 1, pp. 3–30, Jan. 1998, ISSN: 1049-3301. DOI: 10.1145/272991.272995. [Online]. Available: https://doi.org/10.1145/272991.272995.

[7] A. J. Pickles, "A Stellar Spectral Flux Library: 1150-25000 Å," **??***jnlPASP*, vol. 110, no. 749, pp. 863–878, Jul. 1998. DOI: 10.1086/316197.

[8] F. Ochsenbein, P. Bauer, and J. Marcout, "The VizieR database of astronomical catalogues," **??***jnlA&As*, vol. 143, pp. 23–32, Apr. 2000. DOI: 10.1051/aas:2000169. arXiv: astro-ph/0002122 [astro-ph].

[9] E. E. Mamajek, M. R. Meyer, and J. Liebert, "Post-T Tauri Stars in the Nearest OB Association," **??***jnlAJ*, vol. 124, no. 3, pp. 1670–1694, Sep. 2002. DOI: 10.1086/341952. arXiv: astro-ph/0205417 [astro-ph].

[10] K. M. Górski, E. Hivon, A. J. Banday, *et al.*, "HEALPix: A Framework for High-Resolution Discretization and Fast Analysis of Data Distributed on the Sphere," **??***jnlApJ*, vol. 622, no. 2, pp. 759–771, Apr. 2005. DOI: 10.1086/427976. arXiv: astro-ph/0409513 [astro-ph].

[11] I. Antcheva, M. Ballintijn, B. Bellenot, *et al.*, "Root — a c++ framework for petabyte data storage, statistical analysis and visualization," *Computer Physics Communications*, vol. 180, no. 12, pp. 2499–2512, 2009, 40 YEARS OF CPC: A celebratory issue focused on quality software for high performance, grid and novel computing architectures, ISSN: 0010-4655. DOI: https://doi.org/10.1016/j.cpc.2009.08.005. [Online]. Available: https://www.sciencedirect.com/science/article/pii/S0010465509002550.

[12] M. Beaumel, D. Hervé, and D. Van Aken, "Cobalt-60, proton and electron irradiation of a radiation-hardened active pixel sensor," *IEEE Transactions on Nuclear Science*, vol. 57, no. 4, pp. 2056–2065, 2010. DOI: 10.1109/TNS.2010.2048043.

[13] G. Worthey and H.-c. Lee, "An Empirical UBV RI JHK Color-Temperature Calibration for Stars," **??***jnlApJS*, vol. 193, no. 1, 1, p. 1, Mar. 2011. DOI: 10.1088/0067-0049/193/1/1. arXiv: astro-ph/0604590 [astro-ph].

[14] M. Koleva and A. Vazdekis, "Stellar population models in the UV. I. Characterisation of the New Generation Stellar Library," **??***jnlA&A*, vol. 538, A143, A143, Feb. 2012. DOI: 10.1051/0004-6361/201118065. arXiv: 1111.5449 [astro-ph.CO].

[15] Astropy Collaboration, T. P. Robitaille, E. J. Tollerud, *et al.*, "Astropy: A community Python package for astronomy," **??***jnlA&A*, vol. 558, A33, A33, Oct. 2013. DOI: 10.1051/0004-6361/201322068. arXiv: 1307.6212 [astro-ph.IM].

[16] M. Cesetti, A. Pizzella, V. D. Ivanov, L. Morelli, E. M. Corsini, and E. Dalla Bontà, "The Infrared Telescope Facility (IRTF) spectral library:. Spectral diagnostics for cool stars," **??***jnlA&A*, vol. 549, A129, A129, Jan. 2013. DOI: 10.1051/0004-6361/201219078. arXiv: 1211.5572 [astro-ph.SR].

[17] D. Piot and et. al., "Hydra star tracker on-board spot6," *AAS13-046*, 2013.

[18] L. Nicollet and et. al., "Design of a vision-based navigation camera for juice," *GNC ESA 17*, 2017.

[19] Astropy Collaboration, A. M. Price-Whelan, B. M. Sipőcz, *et al.*, "The Astropy Project: Building an Open-science Project and Status of the v2.0 Core Package," **??***jnlAJ*, vol. 156, no. 3, 123, p. 123, Sep. 2018. DOI: 10.3847/1538-3881/aabc4f. arXiv: 1801.02634 [astro-ph.IM].

[20] R. Brochard, J. Lebreton, C. Robin, *et al.*, "Scientific image rendering for space scenes with the SurRender software," *arXiv e-prints*, arXiv:1810.01423, arXiv:1810.01423, Oct. 2018. arXiv: 1810.01423 [astro-ph.IM].

[21] B. Gelin and et. al., "Auriga a reliable and affordable star tracker for constellations and small satellite missions," *AAS 19-122*, 2019.

[22] D. Piot and et. al., "Auriga star tracker flight heritage on inaugural airbus oneweb satellites constellation," *AAS 20-037*, 2020.

[23] D. Piot, L. Oddos Marcel, and et. al., "Auriga star tracker oneweb and angels flight heritage," *GNC ESA 126*, 2020.

[24] F. Gorog and et. al., "Juice navigation camera design," *ESA GNC 21*, 2021.

[25] G. Dubroca, G. Singer, X. Chauffleur, M. Richert, A. Durieux, and A. Lecocq, "Straylight minimization in the design of the ero narrow angle camera," *Proceedings of the International Conference on Space Optics (ICSO)*, 2022.

[26] F. Fullenbaum and et. al., "Horus: A star tracker for space super highways," *AAS23-xxx (submitted)*, 2023.

[27] B. Gelin and et. al., "Horus star tracker," *AAS23-134 (submitted)*, 2023.